JACS
JOURNAL OF THE AMERICAN CHEMICAL SOCIETY
Article
pubs.acs.org/JACS

# Defects Are Needed for Fast Photo-Induced Electron Transfer from a Nanocrystal to a Molecule: Time-Domain *Ab Initio* Analysis

Run Long,[†,§,‡] Niall J. English,[§] and Oleg V. Prezhdo*[,‡]

[†]School of Physics, Complex and Adaptive Systems Laboratory and [§]The SEC Research Cluster, School of Chemical and Bioprocess Engineering, University College Dublin, Belfield, Dublin 4, Ireland

[‡]Department of Chemistry, University of Rochester, Rochester, New York 14627, United States

Supporting Information

**ABSTRACT:** Quantum dot (QD) solar cells constitute an attractive alternative to traditional solar cells due to unique electronic and optical properties of QDs. In order to achieve high photon-to-electron conversion efficiency, rapid charge separation and slow charge recombination are required. We use nonadiabatic molecular dynamics combined with time-domain density functional theory to study electron transfer from a PbS QD to the rhodamine B (RhB) molecule and subsequent electron return from RhB to the QD. The time scale for the electron−hole recombination obtained for the system without defects agrees well with the experiment, while the simulated time scale for the charge separation is 10-fold longer than the experimental value. By performing an atomistic simulation with a sulfur vacancy, which is a common defect in PbS systems, we demonstrate that the defect accelerates the charge separation. This result is supported further by scaling arguments. Missing sulfur creates unsaturated chemical bonds on Pb atoms, which form the PbS conduction band. As a result, the QD lowest unoccupied molecular orbital (LUMO) is lowered in energy, and the LUMO density extends onto the adsorbed molecule, increasing the donor−acceptor interaction. The counterintuitive conclusion that defects are essential rather than detrimental to functioning of QD solar cells generates an unexpected view on the QD surface chemistry.

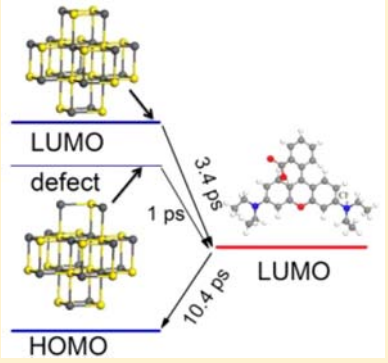


## 1. INTRODUCTION

Quantum dot (QD) solar cells (SCs) have the potential to increase the maximum attainable thermodynamic efficiency of solar photon conversion by utilizing hot photogenerated carriers to produce higher photovoltages and photocurrents. Large absorption cross sections and easily tunable spectral features provide QDs with additional advantages compared to molecular chromophores. QDs made of lead salts, including PbS, PbSe, and PbTe, have been investigated intensely because of their unique photophysical properties, including broad spectral response, extending from visible to near-IR,[1] and long exciton lifetimes.[2,3] The small band gap of bulk lead salts allows one to utilize quantum confinement and tune QD absorbance over the entire solar spectrum via changes in QD size and shape. The interplay between the electron−phonon relaxation dynamics in QDs has received particular attention.[4−24] Hot-carrier generation and carrier multiplication open new ways to improve conversion efficiencies of QD solar cells by reducing the loss of high-energy carriers.[25] Recently, Zhu and coauthors[26] reported ultrafast transfer of hot excited electrons from PbSe QDs into the $TiO_2$ semiconductor. The time-domain *ab initio* analysis of the experimental results was given in ref 27. Shortly after, Parkinson and co-workers[24] and Nozik and co-workers[28] reported photocurrent enhancement in QD-sensitized $TiO_2$ semiconductors, arising due to carrier multiplication. The experiments imply that the rates of electron transfer involving PbSe and PbS QDs are faster than the exciton−exciton annihilation (10−100 ps)[29,30] and are competitive with hot electron relaxation (~0.2−6 ps).[31,32] These experimental findings give strong motivation to the development of QD-based solar cells.

Molecular electron acceptors provide an alternative route to photogenerated charge extraction from semiconductor QDs.[33−37] While bulk semiconductors, such as $TiO_2$, are connected to QDs via intermediate species, for instance, ligands present on surfaces of colloidal QDs, molecular electron acceptors can be bound to QDs directly. The direct contact should facilitate charge separation, improving the competition with charge-phonon energy losses. Lian and co-workers reported a transient absorption study of charge carrier separation and recombination between PbS QDs and an adsorbed electron acceptor, methylene blue ($MB^+$).[35] They found that electron transfer from the QD donor to the $MB^+$ acceptor occurs faster than the recombination, with the characteristic times of 0.36 and 9 ps, respectively. Similar studies have been carried out with other systems. For example, a 2 ps electron transfer has been reported from CdSe QDs to $MB^{+}$[7] and Rebipyridyl[36] molecules. A 12 ps time scale was found for electron transfer from CdS QDs to the rhodamine B (RhB) molecule.[37] The different rates of experimentally observed charge separation and recombination likely arise due

**Received:** August 29, 2013
**Published:** November 26, 2013

   dx.doi.org/10.1021/ja408936j | J. Am. Chem. Soc. 2013, 135, 18892−18900

to diversity in the donor−acceptor energetics, chemical bonding, and coupling strengths among these systems.

Charge separation is central for sunlight-to-electricity conversion in solar cells. Electron−hole dissociation competes with deactivation processes, such as phonon-induced exciton and charge relaxation and electron−hole recombination. The relaxation diminishes the attainable voltage, while the recombination reduces the current. For optimal device performance, the injection must be significantly faster than the de-excitation channels. Therefore, the experimental finding,[35] showing that the PbS QD-$MB^+$ composites exhibit rapid 0.36 ps charge separation and slow 9 ps recombination, makes this system a promising photovoltaic material. Direct time-domain simulation of photoinduced dynamics in the PbS QD-$MB^+$ system is problematic because it is charged and there is no covalent bonding between the QD and the molecule, as discussed in more detail below. Instead, we employ the neutral RhB molecule that is bound to the QD via the carboxylic acid group. Similarly to $MB^+$, RhB is used for extraction of photoexcited electrons from QDs.[37] Furthermore, the electronic structure of RhB-QD is analogous to that of $MB^+$-QD. Selection of a suitable simulation model is often used to explore charge transfer dynamics while saving computational cost.[38]

An atomistic understanding of the photoinduced charge separation and recombination at the interfaces between semiconductor QDs and molecular electron acceptors is required, in order to generate critical insights into the photovoltaic systems and to provide valuable guidelines for material design and improvement. Nonadiabatic (NA)[39] molecular dynamics (MD) combined with time-domain Kohn−Sham (TDKS) density functional theory (DFT) developed in our group[27,40−44] constitutes one of the best theoretical tools currently available for this purpose. Other techniques, such as the recently developed semiclassical Monte Carlo approach,[45] provide alternative approaches that can be used to study NA dynamics in extended molecular systems and solids. The time-domain *ab initio* description generated by NAMD-TDKS allows us to establish the mechanisms of electron injection, relaxation, and recombination, to study dependence of these processes on atomistic details, such as the donor−acceptor binding, and to avoid empirical parameters needed in phenomenological theories. The simulations assist in interpretation of the experimental data and complement analyses based on reaction rate theories, such as the Marcus theory and Fermi's golden rule.

The Theoretical Methodologies section presents the essential theoretical background and computational details of the simulation. The Results and Discussion section considers the geometric and electronic structure of the PbS QD-RhB system, followed by an analysis of the nuclear dynamics and electron-vibrational interactions, and a detailed examination of the charge separation and recombination processes. The simulation results are compared with the available experimental data. The paper concludes with a summary of the most important findings.

## 2. THEORETICAL METHODOLOGIES

The simulations utilize the quantum classical fewest-switches surface hopping (FSSH) technique[46] implemented within the time-dependent KS scheme.[47−49] The approach has been verified with many systems and processes, including electron transfer at $TiO_2$ interfaces with molecular chromophores,[40−42] water,[43] semiconductor QDs,[27] and graphene[44] as well as electron−phonon relaxation in carbon nanotubes,[50−52] graphane,[53] and semiconductor and metallic QDs.[54−59] The approach provides a detailed *ab initio* picture of the coupled electron-vibrational dynamics at the atomistic scale and in the time domain, mimicking the time-resolved experiments as closely as possible. After an initial excitation, the simulated system is allowed to evolve in the electronic-state manifold coupled to semiclassical phonons.

**2.1. Time-Domain DFT.** Time-domain DFT (TDDFT)[60] relates electronic properties of a system to the electron density, expressed by the sum of the densities of the occupied time-dependent single-electron KS orbitals, $\varphi_p(\mathbf{r}, t)$:

$$\rho(\mathbf{r}, t) = \sum_{p=1}^{N_e} \left|\varphi_p(\mathbf{r}, t)\right|^2 \tag{1}$$

where $N_e$ is the number of electrons. The evolution of $\varphi_p(\mathbf{r}, t)$ is determined by application of the time-dependent variational principle to the expectation value of the KS density functional. It gives a set of single-particle equations for the evolution of the KS orbitals:[49,61]

$$i\hbar\frac{\partial\varphi_p(\mathbf{r}, t)}{\partial t} = H(\mathbf{r}, \mathbf{R}, t)\varphi_p(\mathbf{r}, t); \quad p = 1, 2, ..., N_e \tag{2}$$

These single-electron equations are coupled, because the DFT Hamiltonian $H$ depends on the overall electron density, eq 1. The electron-vibrational coupling enters the Hamiltonian through the external potential created by the nuclei. Expanding the time-dependent KS orbital $\varphi_p(\mathbf{r}, t)$ in the adiabatic KS orbital basis $\tilde{\varphi}_k(\mathbf{r}, \mathbf{R}(t))$

$$\varphi_p(r, t) = \sum c_{pk}(t)\tilde{\varphi}_k(\mathbf{r}; \mathbf{R}(t)) \tag{3}$$

and inserting the expansion into eq 2 gives the equation describing the evolution of the expansion coefficients:[47]

$$i\hbar\frac{\partial}{\partial t}c_{pk}(t) = \sum_{m=1}^{N_e} c_{pm}(t)(\varepsilon_m\delta_{km} + d_{km}\cdot\dot{\mathbf{R}}) \tag{4}$$

The adiabatic KS orbitals are readily available from time-independent DFT calculations, which bear the majority of the computational effort in the current approach. The NA coupling

$$d_{km}\cdot\dot{\mathbf{R}} = -i\hbar\langle\tilde{\varphi}_k|\nabla_{\mathbf{R}}|\tilde{\varphi}_m\rangle\cdot\frac{d\mathbf{R}}{dt} = -i\hbar\left\langle\tilde{\varphi}_k\middle|\frac{\partial}{\partial t}\middle|\tilde{\varphi}_m\right\rangle$$
$$\approx -\frac{i\hbar}{2\Delta t}(\langle\tilde{\varphi}_k(t)|\tilde{\varphi}_m(t+\Delta t)\rangle - \langle\tilde{\varphi}_k(t+\Delta t)|\tilde{\varphi}_m(t)\rangle) \tag{5}$$

arises from the dependence of the adiabatic KS orbitals on the atomic coordinates. It is calculated numerically as the overlap of orbitals at sequential steps[62] using eq 5.

**2.2. Fewest Switches Surface Hopping (FSSH).** FSSH is an algorithm for modeling dynamics of mixed quantum classical systems.[46,62] The algorithm was implemented within TDKS theory in ref 47, tested in ref 48, and applied to a number of nanoscale systems.[44,50−58,63,64] FSSH provides a probability for hopping between quantum states based on the evolution of the expansion coefficients, eq 4. The probability of a transition from state $k$ to another state $m$ within the time interval $\delta t$ is given in FSSH by[46]

$$dP_{km} = \frac{b_{km}}{a_{kk}}dt \quad (6)$$

where

$$b_{km} = -2\mathrm{Re}(a^*_{km}\mathbf{d}_{km}\cdot\dot{\mathbf{R}}); \qquad a_{km} = c_k c^*_m$$

If the calculated $dP_{km}$ is negative, the hopping probability is set to zero; a hop from state $k$ to state $m$ can take place only when the electronic occupation of state $k$ decreases and the occupation of state $m$ increases. To conserve the total electron−nuclear energy after a hop, the original FSSH technique rescales the nuclear velocities along the direction of the NA coupling. If a NA transition to a higher energy electronic state is predicted by eq 6, but the kinetic energy available in the nuclear coordinates along the direction of the NA coupling is insufficient to accommodate the increase in the electronic energy, then the hop is rejected. The velocity rescaling and hop rejection give rise to the detailed balance between transitions upward and downward in energy.[62] The assumption that the energy exchanged between the electronic and nuclear degrees of freedom during the hop is redistributed rapidly gives Boltzmann distribution of energy among nuclear modes. Then, the velocity rescaling and hop rejection can be replaced by multiplying the probability (eq 6) for transitions upward in energy by the Boltzmann factor.[65,66] This simplification of the original FSSH technique gives great computational savings, allowing us to determine the time-dependent potential that drives multiple FSSH realizations of the dynamics of the electronic subsystem using a single MD trajectory.

**2.3. Simulation Details.** The time-domain *ab initio* simulations of the photoinduced charge separation and subsequent recombination focus on the PbS QD-RhB inorganic−organic composite, Figure 1. The study is motivated

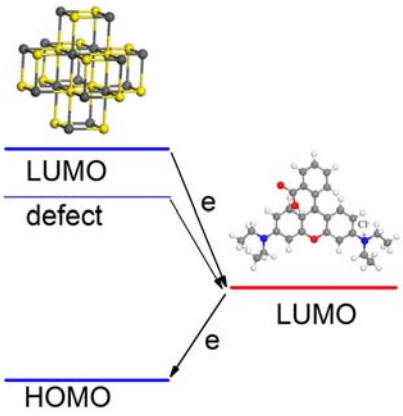


**Figure 1.** Schematic diagram of the energy levels involved in the charge separation and recombination processes in the PbS QD- RhB system. The geometries of the QD and RhB are shown above their corresponding levels.

by the recent experimental results.[35] The $MB^+$ molecule used in experiment is replaced with the RhB molecule for computational convenience. In particular, RhB is a neutral molecule, while $MB^+$ is charged, requiring an explicit counterion or a large solvent representation to compensate or screen the charge. Charge neutrality is an important issue in calculations with periodic setup. Further, binding of the RhB molecule to the QD is well-defined, because it contains the carboxylic acid group. At the same, the binding motif between MB+ and the QD is less obvious. Similarly to $MB^+$, RhB is used for extraction of photoexcited electrons from QDs,[37] and the electronic structure of the QD-RhB system is similar to that of QD-$MB^+$. The simulation cell contains the RhB molecule attached to the $Pb_{16}S_{16}$ QD, as shown in Figure 2. Analogous to the

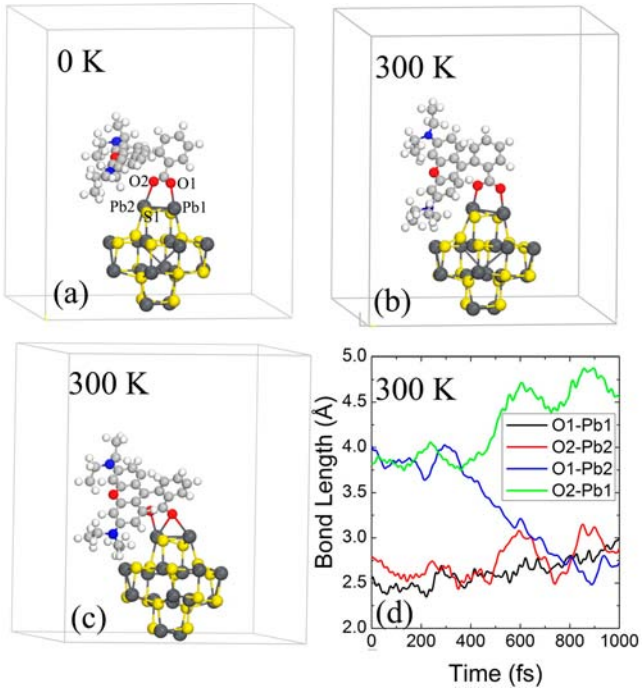


**Figure 2.** Side view of the simulation cell showing the geometry of the PbS QD-RhB system (a) optimized at 0 K and (b, c) during the molecular dynamics run at 300 K. (d) Bond lengths of the covalent links between the O and Pb atoms at the interface. Thermal fluctuations affect the system geometry and, hence, its electronic structure. The changes seen in part (d) are associated with the motion taking the system from geometry shown in part (b) to that in part (c).

binding of Ru(II)-polybipyridine to the PbSe QD,[67] the energetically favorable configuration of the current system involves the two oxygen atoms of the RhB molecule bound to two Pb atoms of the QD.

Geometry optimization, electronic structure, and adiabatic MD calculations were carried out using the Vienna *ab initio* simulation package (VASP).[68] VASP employs a plane-wave basis, allowing for efficient calculation of the electronic kinetic and potential energies with the help of fast Fourier transforms (FTs). The plane-wave basis requires periodic boundary conditions. To avoid interactions between periodic images of the system, it was placed into a large periodic box with dimensions 24 × 24 × 28 Å$^3$. The nonlocal exchange and correlation contributions to the electronic energy were treated with the Perdew−Burke−Ernzerhof (PBE) functional.[69] The projector-augmented wave (PAW) approach was used to describe the interaction of the ionic cores with the valence electrons.[70] After relaxing the geometry at 0 K, Figure 2a, repeated velocity rescaling was used to bring the temperature of the PbS-RhB system to 300 K, corresponding to the temperature in the experiment.[35] Then, a 6 ps adiabatic MD simulation was performed in the microcanonical ensemble with a 1 fs atomic time step. The energies and NA couplings between the two pairs of states, Figure 1, were calculated. The


dx.doi.org/10.1021/ja408936j | J. Am. Chem. Soc. 2013, 135, 18892−18900

densities of states of the PbS QD and the RhB molecule and the optical absorption spectrum of the combined system are presented in Figures S1 and S2. The adiabatic MD trajectory was used to sample the initial conditions and to carry out the NAMD simulations. The TDKS eq 4 was solved using a $10^{-3}$ fs time step. The use of different nuclear and electronic time-steps greatly speeds up the simulation.[71]

## 3. RESULTS AND DISCUSSION

Figure 1 shows a diagram of the energy levels for the photoinduced electron transfer and subsequent electron−hole recombination processes, along with the optimized geometries of the $Pb_{16}S_{16}$ QD and the RhB molecule. Absorption of a photon by the PbS QD excites an electron from the highest occupied molecular orbital (HOMO) to its lowest unoccupied molecular orbital (LUMO). In general, an absorbed photon can create a higher energy electron−hole pair. Rapidly, on a subpicosecond time scale, the electron and hole relax to their lowest states, LUMO and HOMO, respectively, by coupling to phonons. Therefore, the HOMO−LUMO excitation provides the appropriate initial condition for the charge transfer dynamics. The electron moves from the QD LUMO to the RhB LUMO by a NA transition, losing energy to phonons. The electron transfer creates a separated electron−hole pair. Because the pair is spatially separated, the electron−hole interaction energy is weak. One can expect that the interaction energy is less than the binding energy of the exciton arising from the electron and hole confined inside the QD. Subsequently, the electron returns to the QD HOMO, resulting in the electron−hole recombination.

The present work is motivated by the recent experiments[35] showing that the electron extraction from the QD occurs within 0.36 ps, while the electron−hole recombination takes place on a significantly longer, 9 ps time scale. The geometric and electronic structure of the PbS QD-RhB system, the electron−phonon interactions, and the competition between the charge separation and recombination constitute the subject of the current time-domain *ab initio* simulations.

**3.1. Geometric and Electronic Structure of the PbS QD-RhB System.** The interaction between the PbS QD and the RhB molecule determines the rates of charge separation and recombination. In particular, the QD-RhB geometry affects the strength of the donor−acceptor coupling. Figure 2 shows a side view of the system relaxed at 0 K (Figure 2a) and two snapshots taken from the MD run (Figure 2b,c). A comparison of these three panels indicates that thermal fluctuations have a notable impact on the system geometry. The largest-scale motion is associated with rotation of the RhB molecule relative to the QD and bending of the molecule. In the geometry optimized at 0 K, the lengths of the O1−Pb1 and O2−Pb2 bonds are 2.59 and 2.53 Å, respectively (Figure 2a). At room temperature, the bonds shorten to 2.45 and 2.51 Å, respectively, and the molecule rotates relative to the QD (Figure 2b). Further along the trajectory (Figure 2c) the molecule continues to rotate and bend, leading to formation of a new bond between O1 and Pb2 with the length of 2.73 Å. The lengths of the original O1−Pb1 and O2−Pb2 bonds grow and become equal to 3.00 and 2.89 Å, respectively.

In order to reflect the changes of the bond lengths at the interface, Figure 2d depicts the bond lengths for 1 ps along the MD trajectory. The O1−Pb1 and O2−Pb2 bonds fluctuate around the average values. Initially, the O1−Pb2 distance is large and continues to oscillate in the local minimum for the first 300 fs. Then, the distance drops sharply, and the O1−Pb2 bond is formed around 700 fs. The O1−Pb2 distance fluctuates around the new local minimum for the remainder of the shown trajectory. Simultaneously with the decrease of the O1−Pb2 distance, the length of the O2−Pb1 bond increases and then oscillates around a new value. The drawings and data shown in Figure 2a−d clearly show that the molecule undergoes significant bending and rotational motions. At the same time, the structure of the QD changes little, because inorganic nanocrystals are much more rigid than organic chromophores. The involvement of the large-scale motions in the charge-transfer dynamics in the molecule-QD systems is similar to the effect of nuclear dynamics on enzyme catalysis[72] and the role of proton transfer in the proton-coupled electron transfer.[73]

The photoexcitation of the hybrid organic−inorganic system promotes an electron from the QD HOMO to LUMO. Then, the electron relaxes nonadiabatically to the RhB LUMO and finally returns to the QD HOMO, also by a NA transition. Figure 3 presents the charge densities of the three key

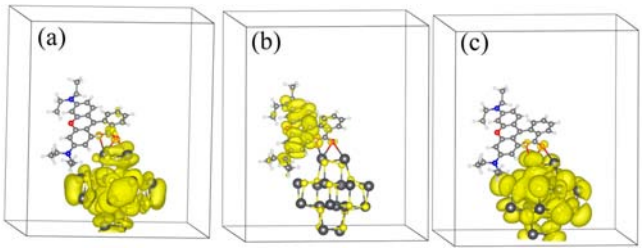


**Figure 3.** Charge densities of (a) QD LUMO, (b) RhB LUMO, and (c) QD HOMO. The QD states are slightly delocalized onto the RhB molecule, enhancing the donor−acceptor coupling and facilitating the charge separation and recombination in the QD-RhB system.

electronic states. The QD LUMO is the donor state (Figure 3a) for the charge separation. It is delocalized slightly on the RhB electron acceptor, providing the donor−acceptor state overlap needed to generate the coupling. The electron-acceptor state (Figure 3b), however, is entirely localized on the LUMO of the RhB molecule. A similar behavior is seen with the charge recombination step: The QD HOMO orbital (Figure 3c) is delocalized slightly onto the RhB molecule, while the molecular state, RhB LUMO, exhibits no discernible delocalization onto the QD. These results are in agreement with the idea that surface ligands increase the effective size of QDs, since QD orbitals extend onto the ligands.[34]

**3.2. Electron-Vibrational Interactions.** Coupling to vibrational motions induces a fluctuation in the electronic energy. Figure 4a shows the evolution of the QD HOMO and LUMO and RhB LUMO over the 1 ps time interval, already used to illustrate fluctuations in the interfacial bond lengths in Figure 2d. The gaps between the QD and RhB LUMOs and between the QD LUMO and RhB HOMO, averaged during the 6 ps MD run, are 1.01 and 0.67 eV, respectively. The relative magnitudes of the gaps agree well with the experimental values of 0.8 and 0.5 eV.[35] The difference arises because we use the RhB molecule, while the experiment employs $MB^+$. As argued earlier, $MB^+$ is harder to simulate because it is an ion.

The fluctuations of the energies of the QD LUMO and HOMO are much smaller than the fluctuation of the RhB LUMO energy. This is reasonable because the QD is composed of heavy atoms and exhibits high symmetry. Heavy atoms move little, and the QD symmetry is approximately preserved. In


dx.doi.org/10.1021/ja408936j | J. Am. Chem. Soc. 2013, 135, 18892−18900

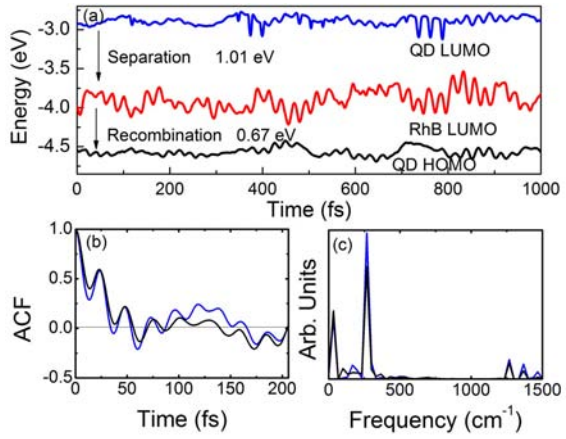


**Figure 4.** (a) Evolution of the energies of the QD LUMO (blue line) and HOMO (black line) and RhB LUMO (red line). The molecular level fluctuates more than the QD levels, because the QD is more rigid and composed of heavier atoms. At certain points in time, e.g., 400–500 fs, the energy fluctuations increase because of a larger scale geometry change, see Figure 2b–d. (b) Autocorrelation functions and (c) FTs of the electronic energy gaps between the QD LUMO and the RhB LUMO (blue line) and between the RhB LUMO and the QD HOMO (black line). The dominant 265 $cm^{-1}$ can be attributed to bending of the RhB molecule (Figure 2) and the second overtone of the longitudinal optical phonon of the PbS QD.[74] The peak at 170 $cm^{-1}$ is close to the PbS mode at 173 $cm^{-1}$ arising from the combined LA and TA modes of PbS.[74] The 33 $cm^{-1}$ peak is due to the TA mode of PbS[74] and the 97 $cm^{-1}$ peak seen in QD HOMO-RhB LUMO FT is due to the Raman-inactive mode of PbS QD.[77] The low-frequency peaks also contain contributions from the hindered rotation of RhB with respect to the QD (Figure 2). The signals in the 1300–1500 $cm^{-1}$ range arise solely from stretching modes of RhB.[78]

contrast, the molecule contains light atoms and possesses low symmetry. The stretching, bending, and rotation of the molecule occurring during the MD run generate a much more significant fluctuation of the RhB LUMO energy compared to the energies of the QD states. Generally, more delocalized states, i.e., those of the QD (Figure 3), exhibit smaller energy fluctuations.

The above analysis indicates that the QD is responsible for the donor–acceptor coupling, while the molecule generates the electron–phonon coupling. The tails of the QD states extend onto the molecule (Figure 3), and therefore, they are responsible for the overlap of the donor and acceptor orbitals. The large fluctuation of the RhB LUMO energy due to nuclear motions indicates strong electron–phonon coupling. Therefore, the electronic energy lost during quantum transitions is accommodated primarily by molecular vibrations.

The increased oscillations of the orbital energies seen in Figure 4a starting at 370 fs correlate with the onset of the changes in the system geometry illustrated in Figure 2. The O2–Pb1 distance starts increasing, while the O1–Pb2 distance starts decreasing at that time. The relatively quiet period in the energy oscillations ensues, corresponding to the RhB rotation with respect to the QD. Around 700 fs the O1 atom approaches the Pb2 atom to the extent allowing formation of a covalent bond. The bond formation event is also associated with an increased amplitude of the orbital energy fluctuations. Thus, formation and dissociation of the secondary bonds between the PbS QD and the RhB molecule increase electron–phonon interactions. During these events, low-frequency vibrational and bending motions of the RhB molecule couple intensely to the high-frequency local modes. The latter induces strong NA coupling, since, according to eq 5, the NA coupling is proportional to the nuclear velocity; and for a given amount of energy, the nuclear velocity is largest for high-frequency modes. The randomness of the phonon-induced fluctuation in the electronic excitation energy gap is characterized by the autocorrelation functions (ACFs). The normalized ACF is defined as

$$C(t) = \frac{\langle E(t)E(0)\rangle}{\langle E^2\rangle} \tag{7}$$

where $E(t)$ is the energy gap between a given pair of states. The ACF describes how the energy at a particular time depends on its value at earlier times. Figure 4b shows the ACFs for the transitions between the QD LUMO and the RhB LUMO (blue line) and between the RhB LUMO and the QD HOMO (black line). Both ACFs decay rapidly to zero within 50 fs and oscillate moderately at longer times. The minor differences between the ACFs should be attributed to the finite duration of the MD simulation. The ACFs are essentially identical within the numerical convergence limits. The rapid decay of the ACFs is a result of coupling of the electronic subsystem with multiple phonon modes. One can expect that the ACF will decay even faster in a larger system, because a broader range of phonon modes will couple to the electronic subsystem and the evolution of the energy gap will be more random.

Vibrational motions of the QD and RhB are directly involved in the charge separation and recombination processes. They both alter the energy gap between the donor and acceptor states (Figure 4a) and create the NA coupling between these states. Figure 4c presents the power spectra, computed as FTs of the energy gaps between the QD LUMO and RhB LUMO (blue line) and the RhB LUMO and the QD HOMO (black line). The FTs characterize the frequencies of the phonon modes that induce the electronic transitions and accommodate the electronic energy lost during the transitions. In both cases, the dominant peak appears at 265 $cm^{-1}$ (Figure 4c). The persistent oscillation seen in the ACF (Figure 4b) corresponds to this peak. It can be attributed to the bending modes of the RhB molecule and to an overtone of the second transverse-optical (2TO) phonon of the PbS QD.[74] The optical phonon frequency for PbS in the Γ-point is equal to 215 $cm^{-1}$, while the spheroidal acoustic mode is around 70 $cm^{-1}$.[75] A combination of these two modes can contribute to the signal dominating the spectra shown in Figure 4c as well.

The second highest signal in the FT shown in Figure 4c appears at a very low frequency, around 50 $cm^{-1}$. It can arise due to both the hindered rotation of the RhB molecule relative to the QD (Figure 2) and spheroidal acoustic modes of the QD. Unlike carrier relaxation dynamics in bulk semiconductors, which is driven only by high-frequency optical phonons, excitation dynamics in nanocrystals is also influenced by acoustic phonons.[76] The NA electron–phonon coupling, eq 5, is determined by the product of the nuclear velocity $d\mathbf{R}/dt$ and the derivative of the electronic wave function with respect to the phonon coordinate, $\langle\tilde{\varphi}_j(r, \mathbf{R})|\nabla_{\mathbf{R}}|\tilde{\varphi}_k(r, \mathbf{R})\rangle$. At a given temperature, higher-frequency modes with lighter effective masses produce larger velocities. Therefore, one can assume *a priori* that high-frequency vibrations should generate stronger electron–phonon coupling. Nevertheless, the electronic contribution, $\langle\tilde{\varphi}_j(r, \mathbf{R})|\nabla_{\mathbf{R}}|\tilde{\varphi}_k(r, \mathbf{R})\rangle$, to the NA coupling tends to be larger for low-frequency acoustic modes. These modes


dx.doi.org/10.1021/ja408936j | J. Am. Chem. Soc. 2013, 135, 18892–18900

modulate size and shape of nanoclusters, thereby greatly affecting the wave function. On the contrary, the positive and negative components of the local displacements of atoms created by optical modes tend to average out during the integration, $<\tilde{\varphi}_j(r, \mathbf{R})|\nabla_{\mathbf{R}}|\tilde{\varphi}_k(r, \mathbf{R})>$, which is performed over delocalized wave functions of the QD. The moderately sized peaks at lower frequencies arise from a series of transverse acoustic (TA) and longitudinal acoustic (LA).[74] The peak at 170 $cm^{-1}$ is close to the PbS mode at 173 $cm^{-1}$ arising from the combined LA + TA mode.[74] The mode at 33 $cm^{-1}$ is directly related to the TA mode of PbS QDs at 38 $cm^{-1}$.[74] The peak around 90 $cm^{-1}$ matches the frequency of the Raman-inactive optical mode.[77]

The highest-frequency signals in the region from 1200 to 1500 $cm^{-1}$ are solely due to the RhB molecule.[78] They correspond to stretching modes of various symmetries involving carbon, oxygen, and nitrogen atoms. Thus, both optical and acoustic modes contribute to the NA electron−phonon coupling, which drives the forward and backward ultrafast charge transfer across the PbS and RhB interface. Considering the mathematical expression for the NA coupling, eq 5, one concludes that the contribution of the high-frequency modes stems primarily from their large velocities, while the contribution of the low-frequency modes arises due to the favorable electron−phonon coupling matrix element.

**3.3. Charge Separation and Recombination Dynamics.** The time-dependent populations of the donor states for the charge separation (QD LUMO) and recombination (RhB LUMO) processes are presented in Figures 5. The data

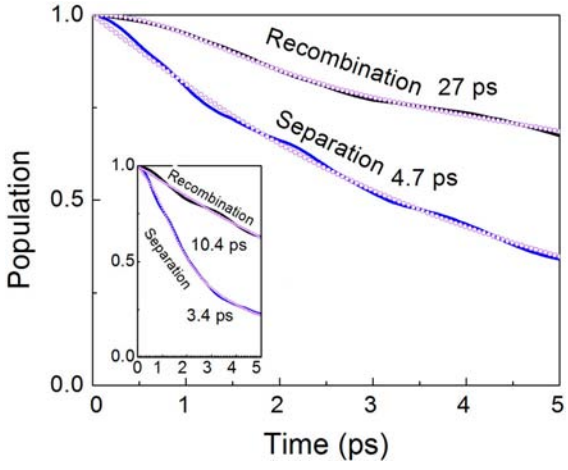


**Figure 5.** Time-dependent populations of the initial states for the charge separation (QD LUMO, blue line) and recombination (RhB LUMO, black line). The inset shows the population decay obtained with the energy gaps rescaled to the experimental values of 0.8 eV for the charge separation and 0.5 eV for the charge recombination. The small circles and times describe the fits, eq 8.

obtained directly from the *ab initio* theory are shown in the main part of Figure 5. The insert in Figure 5 shows the results obtained using the energy gaps scaled to the experimental values for the PbS-$MB^+$ system.[35] In order to obtain the time scales, the data are fitted by a combined exponential and Gaussian function

$$f(t) = B\exp(-t/\tau_1) + (1 - B)\exp(-0.5(t/\tau_2)^2) \quad (8)$$

The times reported in the figures are computed as weighted averages of the exponential and Gaussian components: $\tau = B\tau_1+(1 - B)\tau_2$.

At first, it appears surprising that the charge separation process is faster than the recombination, even though the donor−acceptor energy gap is larger for the separation. For gaps that are significantly larger than the reorganization energy, one expects the exponential gap law,[79] i.e., larger gaps should lead to slower dynamics. The apparent contradiction is rationalized by the difference in the NA coupling values. Recall that the transition rate is proportional to coupling squared, for instance, according to Fermi's golden rule. Canonically averaged at room temperature, the absolute value of the NA coupling between the QD LUMO and the RhB LUMO (5.53 meV) is twice as large as the coupling between the RhB LUMO and the QD HOMO (2.53 meV). A similar relationship exists between the gap root-mean-square values: 4.77 vs 2.85 meV.

The simulated dynamics is slower than the experimental data: The recombination time constant is 3-fold larger in the simulation than in the experiment, and the separation time is some 13-fold larger.[35] The discrepancy may arise due to the differences in the theoretical and experimental energy gaps as well as due to other factors.

In order to compare the simulation to the experiment directly, we rescaled the energy gaps to the experimental values, 0.8 eV for the charge separation and 0.5 eV for the electron−hole recombination, and repeated the NAMD simulations. The time-dependent populations, shown as inset in Figure 5, demonstrate that agreement between theory and experiment is achieved for the charge recombination but not for the charge separation. The 10 ps electron−hole recombination times scale agrees well with 9 ps observed experimentally.[35] The time constant of the charge separation decreases as well, however, it is still about 8 times longer than experiment.[35]

The discrepancy can be attributed to defect states[80] that appear below the edge of the PbS conduction band (CB) and alter both the energy gap and the NA coupling. These kinds of defects are well-known in colloidal QDs and arise due to sulfur vacancies.[81] Surfaces of most optically active QDs are metal rich[82] and, therefore, are missing many sulfur atoms. It should be noted that generally defects on the QD surface can accelerate the electron−hole recombination process as well. However, this can happen only with defects states appearing above the edge of the PbS valence band (VB). Sulfur vacancies do not create such states. Defect states above the PbS VB stem from sulfur-rich surfaces with metal vacancies and interstitial sulfur atoms.[81]

Mimicking the influence of defects states on the photo-induced charge separation in the PbS QD-RhB system, we created a sulfur vacancy in the QD by removing the S1 atom, Figure 2a. The sulfur vacancy lowers the QD LUMO and RhB LUMO energy gap, averaged over the 1 ps trajectory, from 1.01 eV, top panel of Figure 4, to 0.82 eV. The computed root-mean-square value of the NA coupling between the QD LUMO and the RhB LUMO is twice as large in the presence of the defect (9.21 meV) as compared to the ideal system (4.77 meV). The decreased energy gap and increased coupling make the charge separation four times faster, Figure 6, compared to the ideal case, Figure 5. The insert of Figure 6 depicts the charge density of the QD LUMO for the system with the sulfur vacancy. The unsaturated chemical bonds of the Pb atoms, which used to bind to the sulfur atom, contribute strongly to the QD LUMO. Therefore, its density is highest near the


dx.doi.org/10.1021/ja408936j | J. Am. Chem. Soc. 2013, 135, 18892−18900

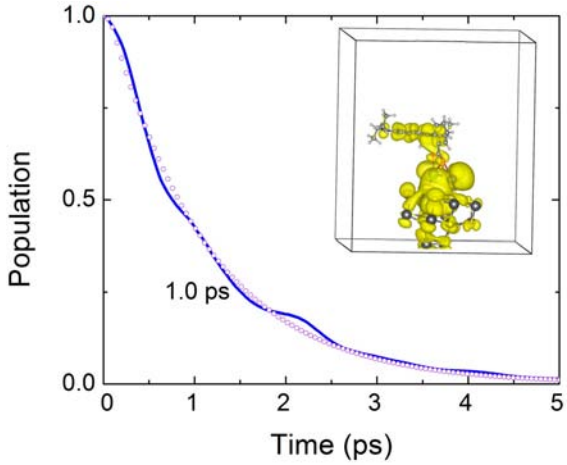


**Figure 6.** Time-dependent populations of the initial state for the charge separation in the system with missing S1 atom, Figure 2a. The inset demonstrates the charge density of the QD LUMO. The density is shifted to the Pb atoms with unsaturated bonds, arising due to the sulfur vacancy, and extends onto the molecule. The donor–acceptor energy gap is decreased by 20%, and the NA coupling is increased by a factor of 2, accelerating the dynamics (cf. Figure 5).

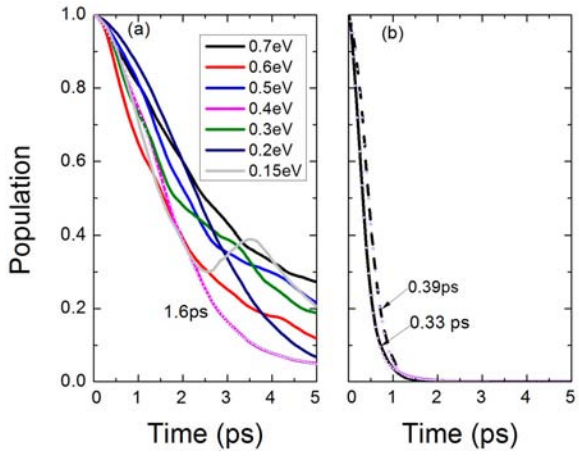


**Figure 7.** Decay of the QD LUMO population during the charge separation process obtained by rescaling (a) the gap between the QD LUMO and RhB LUMO and (b) the NA coupling. The small circles and times represent the fits, eq 8. The goal is to obtain the experimental[35] time scale of 0.36 ps. Reducing the gap mimics defect states, such as sulfur vacancies.[81] The charge separation time decreases as the gap is lowered down to 0.4 eV, part (a). Further lowering of the gap does not speed up the process; rather, it leads to a more complex signal. Increasing the NA coupling 4-fold while keeping the gap at 0.8 eV (solid line) or increasing the NA coupling 3-fold with the 0.4 eV gap (dashed line) matches the experimental time scale. Most likely, defects both reduce the gap and increase the coupling.

missing sulfur. Further, the QD LUMO leaks significantly onto the adsorbed RhB molecule, creating favorable conditions for coupling with the RhB LUMO.

Sulfur vacancies and other defects should have a strong influence on the photoinduced dynamics of systems, such as PbS QD-$MB^+$,[35] without strong chemical binding. The RhB molecule binds to the PbS QD via a relatively strong chemical bond involving the carboxylic acid group. In contrast, $MB^+$ has no functional group designed for the binding. Therefore, the coupling between a stoichiometric QD and $MB^+$ is weaker compared to the RhB case. A sulfur vacancy creates unsaturated chemical bonds on the Pb atoms, which can now bond chemically to $MB^+$ and increase the donor–acceptor coupling. This effect should be less pronounced if a chemical bond between the donor and acceptor species already exists, as in PbS QD-RhB.

The QDs used in the experiments are larger than the simulated QD and likely contain multiple defects. Creating more than one sulfur vacancy in the simulated QD significantly distorts its geometric and electronic structure. In order to investigate how various defects can change the charge separation dynamics, we performed model calculations by starting with the ideal system and scaling either the donor–acceptor energy gap or the NA coupling. First, we assumed that defects reduce the donor–acceptor energy gap and have little influence on the NA coupling. We applied a constant shift to the gap between the RhB LUMO and the QD HOMO from 0.8 to 0.15 eV and repeated the surface hopping dynamics. The electron transfer time decreased from 3.4 ps for the experimental gap of 0.8 eV (insert in Figure 5) to 1.6 ps for the 0.4 eV gap (Figure 7a). Further lowering of the gap did not speed up the dynamics. Rather, the dynamics became more complex, showing oscillatory behavior (Figure 7a).

Since scaling the gap alone failed to bring the simulated results in agreement with the experimental data, we surmised that defects alter both the donor–acceptor energy gap and the NA coupling. This conclusion is supported by the sulfur vacancy simulation and by studies of defects states in carbon nanotubes.[50] Generally, defects create localized states,[82] and more localized electronic excitations generate stronger electron–phonon coupling. By scaling both the donor–acceptor energy gap and the NA coupling, we established that the experimentally measured 0.36 ps charge separation time can be reproduced in different ways. One can keep the gap at the experimental value of 0.8 eV and increase the coupling fourfold. Alternatively, one can decrease the gap, e.g., to 0.4 eV gap and increase the coupling 3-fold. The time scales obtained in these simulations are 0.33 and 0.39 ps, respectively (Figure 7b). The defect states at 0.8 and 0.4 eV can be viewed as shallow and deep traps, respectively. Sulfur vacancies create shallow traps.[81] One can expect that realistic systems exhibit a range of defect states, from shallow to deep. The fact that defects increase the NA electron–phonon coupling by a factor of 3–4 and that the coupling is only weekly dependent on the energy of the defect states agrees with expectations. The NA coupling increases because defect wave functions are more localized than wave functions of ideal QDs. At the same time, the localization of the wave functions by the defects should be approximately independent of the defect energy.

Other factors that may influence the photoinduced dynamics include the QD size and the choice of the DFT functional. Since the energy gaps used in the simulation agree with the experimental data, we need to consider the effect of the QD size and DFT functional on the NA coupling. The NA coupling depends on the overlap of the donor and acceptor wave functions. One can argue that the overlap, and hence the NA coupling, should decrease if the QD size is increased and if one uses a hybrid DFT functional. Increasing the QD size decreases the size of the tail of the QD wave function extending onto the molecule, while hybrid functionals tend to localize states more than pure DFT functionals. Defect states are already localized, and their wave functions should show weak dependence on the QD size and DFT functional.

The finding that defects are needed for efficient photoinduced electron−hole separation is quite surprising, since surface defects are considered detrimental to QD properties,[83] and significant efforts are dedicated to elimination of surface defects by ligand selection, slow QD growth, and other synthetic techniques.

## 4. CONCLUSIONS

By performing time-domain *ab initio* simulations, we investigated the charge separation and recombination processes across the PbS QD-RhB interface and established the factors responsible for the movement of charge through the system. Understanding of these factors is key for successful application of the PbS QD-RhB and related systems in solar light harvesting and utilization. The simulation supports the experimental observation that charge separation is faster than recombination. This order of time scales is surprising, since the donor−acceptor energy gap is smaller for the recombination, and therefore, the recombination should be faster. Already for the pristine system, the simulation shows faster separation than recombination, rationalizing this fact by a twice-stronger NA coupling for the forward than the backward electron transfer reaction. The coupling cannot be measured, and theory provides the only direct route to its evaluation.

The computed electron−hole recombination time scale agreed very well with the experiment result. However, the charge separation time scale was significantly overestimated. The majority of optically active QDs have metal-rich surfaces, and PbS QDs in particular commonly exhibit sulfur vacancies on the surface. We repeated the simulation with a sulfur vacancy defect, achieving good agreement with the experiment. By creating unsaturated chemical bonds on the Pb atoms, which form the PbS conduction band, the sulfur vacancy lowered the QD LUMO energy and enhanced the LUMO delocalization onto the adsorbed molecule. As a result, the donor−acceptor energy gap for the photoinduced charge separation decreased, the NA coupling increased, and the charge separation time shortened further. It is well-known that surface defects reduce the energy gap. A scaling analysis showed that reducing the gap alone could not account for the experimental observation and that defects should enhance the NA coupling. The enhancement of the NA coupling by defect states is approximately independent of the defect state energy.

Both electron separation and electron−hole recombination are NA processes, driven by nuclear vibrational motions. Phonon modes create the NA coupling and accommodate the excess energy released during the quantum transitions. The largest scale atomic motions seen in the simulation involve bending and rotation of the molecule relative to the QD. Occasionally, these low-frequency motions cause an impact between the molecule and the QD, at which time higher-frequency motions are activated. High-frequency modes increase the NA coupling because they generate large nuclear velocities. The NA electron−phonon coupling is created predominantly due to motions of the molecule, because it is composed of lighter atoms and is more labile than the QD. In contrast, the donor−acceptor coupling between the QD and the molecule arises due to the QD, because its wave function leaks onto the adsorbed molecular species, generating the required overlap between the donor and the acceptor wave functions.

The positive involvement of QD surface defects in the photoinduced charge separation changes the current perception that defects are detrimental to functioning of photovoltaic devices. The studied system provides a clear example, in which defects make the charge separation much faster than the charge recombination.

## ■ ASSOCIATED CONTENT

### Supporting Information

Density of states and optical absorption spectrum of the PbS QD-RhB system. This material is available free of charge via the Internet at http://pubs.acs.org.

## ■ AUTHOR INFORMATION

### Corresponding Author

oleg.prezhdo@rochester.edu

### Notes

The authors declare no competing financial interest.

## ■ ACKNOWLEDGMENTS

R.L. is grateful to the SIRG Program 11/SIRG/E2172 of the Science Foundation Ireland, UCD Seed Funding SF895, and IRCSET-Marie Curie International Mobility Fellowship in Science, Engineering, and Technology (reference no. PD/2010/INSP/1485). O.V.P. acknowledges grant DE-SC0006527 from the U.S. Department of Energy.

## ■ REFERENCES

(1) Sargent, E. H. *Nat. Photonics* **2009**, *3*, 325.
(2) Hyun, B.-R.; Zhong, Y.-W.; Bartnik, A. C.; Sun, L.; Abruña, H. D.; Wise, F. W.; Goodreau, J. D.; Matthews, J. R.; Leslie, T. M.; Borrelli, N. F. *ACS Nano* **2008**, *2*, 2206.
(3) Leventis, H. C.; O'Mahony, F.; Akhtar, J.; Afzaal, M.; O'Brien, P.; Haque, S. A. *J. Am. Chem. Soc.* **2010**, *132*, 2743.
(4) Zhu, H.; Song, N.; Rodríguez-Córdoba, W.; Lian, T. *J. Am. Chem. Soc.* **2012**, *134*, 4250.
(5) Zhu, H.; Lian, T. *J. Am. Chem. Soc.* **2012**, *134*, 11289.
(6) Murphy, J. E.; Beard, M. C.; Norman, A. G.; Ahrenkiel, S. P.; Johnson, J. C.; Yu, P.; Mićić, O. I.; Ellingson, R. J.; Nozik, A. J. *J. Am. Chem. Soc.* **2006**, *128*, 3241.
(7) Huang, J.; Huang, Z.; Yang, Y.; Zhu, H.; Lian, T. *J. Am. Chem. Soc.* **2010**, *132*, 4858.
(8) Prezhdo, O. V. *Acc. Chem. Res.* **2009**, *42*, 2005.
(9) Schaller, R. D.; Klimov, V. I. *Phys. Rev. Lett.* **2004**, *92*, 186601.
(10) Ellingson, R. J.; Beard, M. C.; Johnson, J. C.; Yu, P.; Micic, O. I.; Nozik, A. J.; Shabaev, A.; Efros, A. L. *Nano Lett.* **2005**, *5*, 865.
(11) Liljeroth, P.; van Emmichoven, P. A. Z.; Hickey, S. G.; Weller, H.; Grandidier, B.; Allan, G.; Vanmaekelbergh, D. *Phys. Rev. Lett.* **2005**, *95*, 086801.
(12) Nozik, A. J.; Beard, M. C.; Luther, J. M.; Law, M.; Ellingson, R. J.; Johnson, J. C. *Chem. Rev.* **2010**, *110*, 6873.
(13) Beard, M. C.; Midgett, A. G.; Hanna, M. C.; Luther, J. M.; Hughes, B. K.; Nozik, A. J. *Nano Lett.* **2010**, *10*, 3019.
(14) McGuire, J. A.; Joo, J.; Pietryga, J. M.; Schaller, R. D.; Klimov, V. I. *Acc. Chem. Res.* **2008**, *41*, 1810.
(15) Nair, G.; Chang, L.-Y.; Geyer, S. M.; Bawendi, M. G. *Nano Lett.* **2011**, *11*, 2145.
(16) Pijpers, J. J. H.; Ulbricht, R.; Tielrooij, K. J.; Osherov, A.; Golan, Y.; Delerue, C.; Allan, G.; Bonn, M. *Nat Phys* **2009**, *5*, 811.
(17) Pandey, A.; Guyot-Sionnest, P. *Science* **2008**, *322*, 929.
(18) Efros, A. L.; Rosen, M. *Annu. Rev. Mater. Sci.* **2000**, *30*, 475.
(19) Califano, M.; Franceschetti, A.; Zunger, A. *Nano Lett.* **2005**, *5*, 2360.
(20) Califano, M.; Zunger, A.; Franceschetti, A. *Nano Lett.* **2004**, *4*, 525.
(21) Rabani, E.; Baer, R. *Nano Lett.* **2008**, *8*, 4488.
(22) Rabani, E.; Baer, R. *Chem. Phys. Lett.* **2010**, *496*, 227.

(23) Kilina, S.; Ivanov, S.; Tretiak, S. *J. Am. Chem. Soc.* **2009**, *131*, 7717.
(24) Sambur, J. B.; Novet, T.; Parkinson, B. A. *Science* **2010**, *330*, 63.
(25) Nozik, A. J. *Phys. E (Amsterdam, Neth.)* **2002**, *14*, 115.
(26) Tisdale, W. A.; Williams, K. J.; Timp, B. A.; Norris, D. J.; Aydil, E. S.; Zhu, X.-Y. *Science* **2010**, *328*, 1543.
(27) Long, R.; Prezhdo, O. V. *J. Am. Chem. Soc.* **2011**, *133*, 19240.
(28) Semonin, O. E.; Luther, J. M.; Choi, S.; Chen, H.-Y.; Gao, J.; Nozik, A. J.; Beard, M. C. *Science* **2011**, *334*, 1530.
(29) Schaller, R. D.; Sykora, M.; Pietryga, J. M.; Klimov, V. I. *Nano Lett.* **2006**, *6*, 424.
(30) Klimov, V. I.; McGuire, J. A.; Schaller, R. D.; Rupasov, V. I. *Phys. Rev. B* **2008**, *77*, 195324.
(31) Schaller, R. D.; Pietryga, J. M.; Goupalov, S. V.; Petruska, M. A.; Ivanov, S. A.; Klimov, V. I. *Phys. Rev. Lett.* **2005**, *95*, 196401.
(32) Harbold, J. M.; Du, H.; Krauss, T. D.; Cho, K.-S.; Murray, C. B.; Wise, F. W. *Phys. Rev. B* **2005**, *72*, 195312.
(33) Morris-Cohen, A. J.; Frederick, M. T.; Cass, L. C.; Weiss, E. A. *J. Am. Chem. Soc.* **2011**, *133*, 10146.
(34) Knowles, K. E.; Malicki, M.; Weiss, E. A. *J. Am. Chem. Soc.* **2012**, *134*, 12470.
(35) Yang, Y.; Rodríguez-Córdoba, W.; Lian, T. *J. Am. Chem. Soc.* **2011**, *133*, 9246.
(36) Huang, J.; Stockwell, D.; Huang, Z.; Mohler, D. L.; Lian, T. *J. Am. Chem. Soc.* **2008**, *130*, 5632.
(37) Boulesbaa, A.; Issac, A.; Stockwell, D.; Huang, Z.; Huang, J.; Guo, J.; Lian, T. *J. Am. Chem. Soc.* **2007**, *129*, 15132.
(38) Jailaubekov, A. E.; Willard, A. P.; Tritsch, J. R.; Chan, W.-L.; Sai, N.; Gearba, R.; Kaake, L. G.; Williams, K. J.; Leung, K.; Rossky, P. J.; Zhu, X. Y. *Nat. Mater.* **2013**, *12*, 66.
(39) Jasper, A. W.; Nangia, S.; Zhu, C.; Truhlar, D. G. *Acc. Chem. Res.* **2005**, *39*, 101.
(40) Duncan, W. R.; Craig, C. F.; Prezhdo, O. V. *J. Am. Chem. Soc.* **2007**, *129*, 8528.
(41) Duncan, W. R.; Prezhdo, O. V. *J. Am. Chem. Soc.* **2008**, *130*, 9756.
(42) Duncan, W. R.; Stier, W. M.; Prezhdo, O. V. *J. Am. Chem. Soc.* **2005**, *127*, 7941.
(43) Fischer, S. A.; Duncan, W. R.; Prezhdo, O. V. *J. Am. Chem. Soc.* **2009**, *131*, 15483.
(44) Long, R.; English, N. J.; Prezhdo, O. V. *J. Am. Chem. Soc.* **2012**, *134*, 14238.
(45) Gorshkov, V. N.; Tretiak, S.; Mozyrsky, D. *Nat Commun* 2013, *4*.
(46) Tully, J. C. *J. Chem. Phys.* **1990**, *93*, 1061.
(47) Craig, C. F.; Duncan, W. R.; Prezhdo, O. V. *Phys. Rev. Lett.* **2005**, *95*, 163001.
(48) Fischer, S. A.; Habenicht, B. F.; Madrid, A. B.; Duncan, W. R.; Prezhdo, O. V. *J. Chem. Phys.* **2011**, *134*, 024102.
(49) Kohn, W.; Sham, L. J. *Phys. Rev.* **1965**, *140*, A1133.
(50) Habenicht, B. F.; Prezhdo, O. V. *Phys. Rev. Lett.* **2008**, *100*, 197402.
(51) Habenicht, B. F.; Craig, C. F.; Prezhdo, O. V. *Phys. Rev. Lett.* **2006**, *96*, 187401.
(52) Habenicht, B. F.; Prezhdo, O. V. *J. Am. Chem. Soc.* **2012**, *134*, 15648.
(53) Nelson, T. R.; Prezhdo, O. V. *J. Am. Chem. Soc.* **2013**, *135*, 3702.
(54) Kilina, S. V.; Kilin, D. S.; Prezhdo, O. V. *ACS Nano* **2008**, *3*, 93.
(55) Kilina, S.; Velizhanin, K. A.; Ivanov, S.; Prezhdo, O. V.; Tretiak, S. *ACS Nano* **2012**, *6*, 6515.
(56) Hyeon-Deuk, K.; Prezhdo, O. V. *ACS Nano* **2012**, *6*, 1239.
(57) Hyeon-Deuk, K.; Prezhdo, O. V. *Nano Lett.* **2011**, *11*, 1845.
(58) Kilina, S. V.; Neukirch, A. J.; Habenicht, B. F.; Kilin, D. S.; Prezhdo, O. V. *Phys. Rev. Lett.* **2013**, *110*, 180404.
(59) Neukirch, A. J.; Guo, Z.; Prezhdo, O. V. *J. Phys. Chem. C* **2012**, *116*, 15034.
(60) Runge, E.; Gross, E. K. U. *Phys. Rev. Lett.* **1984**, *52*, 997.
(61) Isborn, C. M.; Li, X.; Tully, J. C. *J. Chem. Phys.* **2007**, *126*, 134307.
(62) Parandekar, P. V.; Tully, J. C. *J. Chem. Phys.* **2005**, *122*, 094102.
(63) Chaban, V. V.; Prezhdo, V. V.; Prezhdo, O. V. *J. Phys. Chem. Lett.* **2012**, *4*, 1.
(64) Akimov, A. V.; Muckerman, J. T.; Prezhdo, O. V. *J. Am. Chem. Soc.* **2013**, *135*, 8682.
(65) Prezhdo, O. V.; Duncan, W. R.; Prezhdo, V. V. *Prog. Surf. Sci.* **2009**, *84*, 30.
(66) Akimov, A. V.; Prezhdo, O. V. *J. Chem. Theory Comput.* **2013**, *9*, 4959.
(67) Hedrick, M. M.; Mayo, M. L.; Badaeva, E.; Kilina, S. *J. Phys. Chem. C* **2013**, *117*, 18216.
(68) Kresse, G.; Furthmüller, J. *Phys. Rev. B* **1996**, *54*, 11169.
(69) Perdew, J. P.; Burke, K.; Ernzerhof, M. *Phys. Rev. Lett.* **1996**, *77*, 3865.
(70) Blöchl, P. E. *Phys. Rev. B* **1994**, *50*, 17953.
(71) Steele, R. P. *J. Chem. Phys.* **2013**, *139*, 121909.
(72) Henzler-Wildman, K. A.; Lei, M.; Thai, V.; Kerns, S. J.; Karplus, M.; Kern, D. *Nature* **2007**, *450*, 913.
(73) Weinberg, D. R.; Gagliardi, C. J.; Hull, J. F.; Murphy, C. F.; Kent, C. A.; Westlake, B. C.; Paul, A.; Ess, D. H.; McCafferty, D. G.; Meyer, T. J. *Chem. Rev.* **2012**, *112*, 4016.
(74) Milekhin, A. G.; Sveshnikova, L. L.; Duda, T. A.; Surovtsev, N. V.; Adichtchev, S. V.; Azhniuk, Y. M.; Himcinschi, C.; Kehr, M.; Zahn, D. R. T. *J. Phys: Conf. Ser.* **2010**, *245*, 4.
(75) Krauss, T. D.; Wise, F. W. *Phys. Rev. Lett.* **1997**, *79*, 5102.
(76) Woggon, U.; Giessen, H.; Gindele, F.; Wind, O.; Fluegel, B.; Peyghambarian, N. *Phys. Rev. B* **1996**, *54*, 17681.
(77) Machol, J. L.; Wise, F. W.; Patel, R. C.; Tanner, D. B. *Phys. Rev. B* **1993**, *48*, 2819.
(78) Luo, Z. X. F.; Yao, J. N. *Trends Appl. Sci. Res.* **2007**, *2*, 295.
(79) Englman, R.; Jortner, J. *Mol. Phys.* **1970**, *18*, 145.
(80) Inerbaev, T. M.; Masunov, A. E.; Khondaker, S. I.; Dobrinescu, A.; Plamada, A. V.; Kawazoe, Y. *J. Chem. Phys.* **2009**, *131*, 044106.
(81) Xu, X.; Zhao, Y.; Sie, E. J.; Lu, Y.; Liu, B.; Ekahana, S. A.; Ju, X.; Jiang, Q.; Wang, J.; Sun, H.; Sum, T. C.; Huan, C. H. A.; Feng, Y. P.; Xiong, Q. *ACS Nano* **2011**, *5*, 3660.
(82) Wei, H. H.-Y.; Evans, C. M.; Swartz, B. D.; Neukirch, A. J.; Young, J.; Prezhdo, O. V.; Krauss, T. D. *Nano Lett.* **2012**, *12*, 4465.
(83) Zheng, J.; Huang, F.; Yin, S.; Wang, Y.; Lin, Z.; Wu, X.; Zhao, Y. *J. Am. Chem. Soc.* **2010**, *132*, 9528.